UNIVERSITY OF OXFORD
OCCAM
OXFORD CENTRE FOR COLLABORATIVE APPLIED MATHEMATICS

On the mechanics of thin films and growing surfaces

by

Maria A. Holland
Tim Kosmata
Alain Goriely
Ellen Kuhl

OCCAM Preprint Number 13/03

On the mechanics of thin films and growing surfaces

Maria A. Holland[a], Tim Kosmata[a], Alain Goriely[b], Ellen Kuhl[c]

[a] *Department of Mechanical Engineering, Stanford University, Stanford, USA*
[b] *Mathematical Institute, University of Oxford, Oxford, UK*
[c] *Departments of Mechanical Engineering, Bioengineering, and Cardiothoracic Surgery, Stanford University, Stanford, USA*

Abstract

Many living structured are coated by thin films, which have distinct mechanical properties from the bulk. In particular, these thin layers may grow faster or slower than the inner core. Differential growth creates a balanced interplay between tension and compression and plays a critical role in enhancing structural rigidity. Typical examples with a compressive outer surface and a tensile inner core are the petioles of celery, caladium, or rhubarb. While plant physiologists have studied the impact of tissue tension on plant rigidity for more than a century, the fundamental theory of growing surfaces remains poorly understood. Here, we establish a theoretical and computational framework for continua with growing surfaces and demonstrate its application to classical phenomena in plant growth. To allow the surface to grow independently of the bulk, we equip it with its own potential energy and its own surface stress. We derive the governing equations for growing surfaces of zero thickness and obtain their spatial discretization using the finite element method. To illustrate the features of our new surface growth model we simulate the effects of growth-induced longitudinal tissue tension in a stalk of rhubarb. Our results demonstrate that different growth rates create a mechanical environment of axial tissue tension and residual stress, which can be released by peeling off the outer layer. Our novel framework for continua with growing surfaces has immediate biomedical applications beyond these classical model problems in botany: It can be easily extended to model and predict surface growth in asthma, gastritis, obstructive sleep apnoea, brain development, and tumor invasion. Beyond biology and medicine, surface growth models are valuable tools for material scientists when designing functionalized surfaces with distinct user-defined properties.

Keywords: boundary energy, surface growth, thin films, plant growth, finite elements

---

1. Introduction

The phenomenon of growing surfaces has been known to developmental biologists for more than a century [41]. In plant biology, surface growth plays a critical role in creating form and function through the balanced interplay between tension and compression [10]. Surface growth generates a mechanical environment of residual stress, stress that is present even in the absence of external loading [39]. Plant biologists refer to this phenomenon as tissue tension [1].

Figure 1 illustrates growth-induced longitudinal tissue tension in the petiole, the stalk, of *Rheum rhabarbarum*, commonly known as rhubarb [10]. In most plants, the epithelial cells of the outer

---

Email address: `corresponding author` (Ellen Kuhl)
URL: `http://biomechanics.stanford.edu` (Ellen Kuhl)

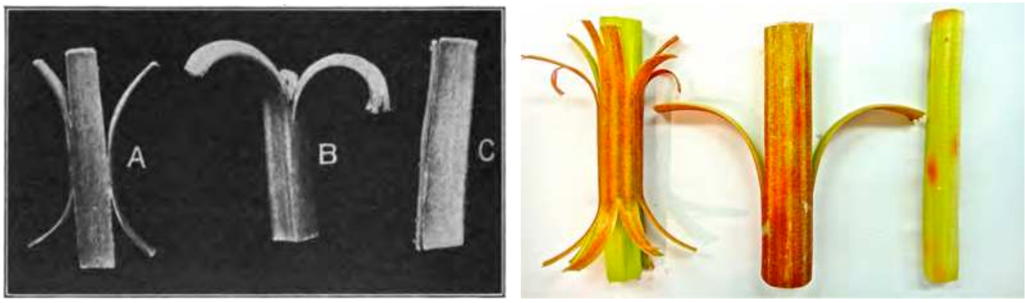

Figure 1: Growth-induced longitudinal tissue tension in a stalk of rhubarb. The red outer surface of the stalk grows slower than the green inner core and generates a state of surface tension and bulk compression. The balanced interplay between tension and compression gives the stalk its characteristic rigidity. When the surface layers are peeled off the inner core, they contract and bend outward, while the inner core expands as tissue tension is released. The release of tissue tension is associated with a significant loss of rigidity, adopted from [10].

surface, shown in red, grow slower than the parenchyma cells of the inner core, shown in green [53]. Differential growth creates a state of surface tension and bulk compression [8], which gives the stalk its characteristic rigidity to support the heavy rhubarb leaves [41]. When the surface layers are peeled off the inner core, they contract and bend outward, while the inner core expands as tissue tension is released. Bending and curvature changes in the classical split pea test have played an important role in the discovery of the plant growth hormone auxin [51], and are one of the major topics in many introductory textbooks on botany [1].

Figure 2 illustrates the microstructure of growing rhubarb. The outer surface, shown in red, consists of a continuous layer of densely packed, brick-shaped epidermal cells, while the inner core, shown in green, consists primarily of thin-walled parenchyma cells and longitudinal fibers. Epidermal cells display a distinct behavior from parenchyma cells [53]; in particular, they grow at a different rate [35]. In cylindrical plant stems, different growth rates generate longitudinal tissue tension, or, in mechanical terms, a state of residual stress [54].

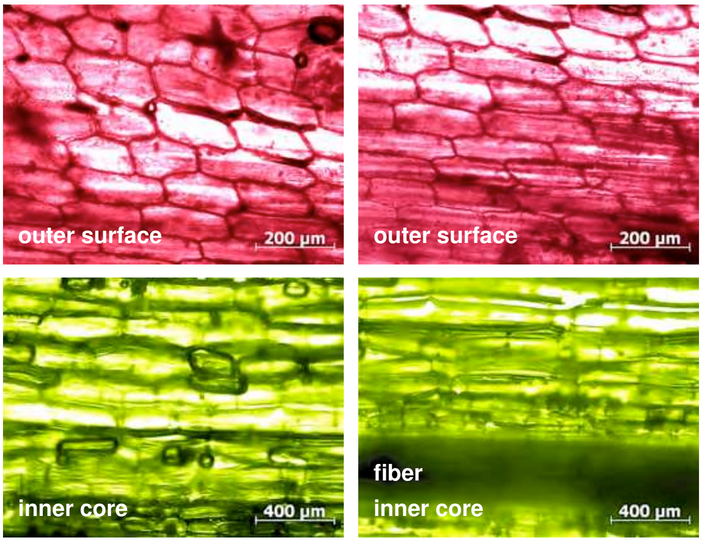

Figure 2: Microstructure of growing rhubarb. The red outer surface consist of epidermal cells; the green inner core consists primarily of parenchyma cells and longitudinal fibers. The epithelial cells of the outer surface grow slower than the parenchyma cells of the inner core creating a state of longitudinal tissue tension to enhance stalk rigidity.

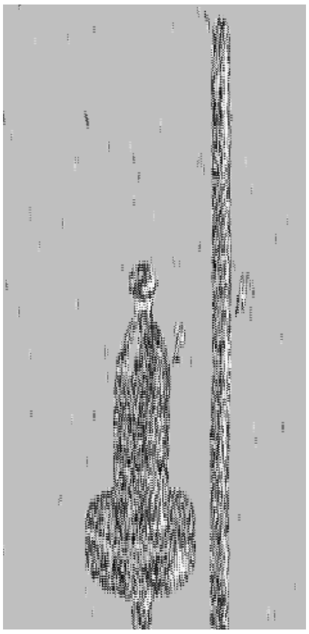

Figure 3: Compression test to quantify residual stresses in rhubarb. When peeling off the outer epidermal surface, the inner parenchyma core expands as growth-induced residual stresses are released. To quantify the amount of residual stress, the parenchyma core is mounted into the tissue holder *B* and loaded by the weight *P*. The weight *P* is calibrated such that the pith recovers its initial length, and is thus a direct measure of the overall residual stress, adopted from [34].

Figure 3 shows a classic experiment to characterize residual stresses in rhubarb. After peeling off the outer epidermal surface, the expanding parenchyma core is mounted into the tissue holder *B* and loaded by the weight *P*. The weight is calibrated such that the pith recovers its initial length, and is thus a direct measure of the overall residual stress [34]. In continuum mechanics, the phenomenon of residual stress is inherently related to the notion of growth [30, 50]. The first continuum model to characterize the interplay between growth and residual stress was proposed almost two decades ago [40]. Motivated by the introduction of an incompatible growth configuration [25], it is based on the multiplicative decomposition of the deformation gradient into a reversible elastic part and an irreversible growth part [4]. In the most generic sense, this growth part can be represented through a second order tensor [11]. Two key ingredients determine the particular type of growth: the functional form of the growth tensor and the driving force for its evolution [13]. The functional form of the growth tensor typically depends on the underlying tissue microstructure [31, 49]. In the simplest case, growth is isotropic [2, 18]. In the presence of fibers, like in rhubarb, growth is typically transversely isotropic, with a pronounced growth or shrinkage along the fiber direction [37, 60]. Area growth is also usually transversely isotropic, i.e., isotropic in the plane tangent to the surface [7, 44]. In complex tissues with multiple fiber families growth can be orthotropic [12], or even generally anisotropic [29]. The driving force for growth can either be morphogenetic, mechanic, or a combination of both. In evolution and developmental biology, the growth process is usually prescribed morphogenetically [55]. This implies that growth and mechanics are only coupled unidirectionally: growth influences mechanics, but mechanics does not influence growth [5, 15]. In biomechanics, the growth process is typically driven by strain [58], stress [23], or energy. This implies that growth and mechanics are coupled bidirectionally: growth influences mechanics, and, at the same time, mechanics influences growth [3, 9]. Motivated by the differential growth in plant stems in Figure 1, here, we focus on transversely isotropic growing surfaces and prescribe the evolution of growth through morphogenesis.

The distinguishing feature of the type of growth we are interested in here is that the growing surface is extremely thin as compared to the bulk [48]. As indicated in Figure 2, many biological structures are coated by of a thin film of epidermal cells with a thickness on the order of micrometers. The modeling of thin films is conceptually challenging and has attracted increased attention within the past two decades. An elegant way to model thin growing surfaces at the zero-thickness limit [32, 45] is to equip the surface with its own potential energy, which can evolve independently of the bulk [36]. The concept of surface energies has been established more than two centuries ago, formalized through the famous Young Laplace equation, which relates the pressure difference across a fluid surface to surface tension and mean curvature [24, 57]. More than three decades ago, the familiar concept of scalar-valued surface tension was generalized to the tensorial notion of surface stress in the first continuum theory of elastic material surfaces [16]. Since then, the concept of material surfaces has gained wide attention in various fields of metallurgy, material sciences, micro- and nanofabrication, and soft lithography [43], broadly speaking, whenever the surface displays distinct characteristic properties [17, 46]. For fluids, the theory of surface tension is classic and well-developed. Computationally, finite element formulations exist to simulate droplets and free surfaces with scalar-valued surface tension [42]. For solids, however, a generic finite element approach towards elastic surfaces with tensorial surface stresses has only been proposed recently [19]. This approach models the surface as a hyperelastic membrane of zero thickness, kinematically constrained to move with the solid body, but equipped with its own potential energy [47]. The concept of surface energies is mathematically elegant and easily generalizable to anisotropic surfaces [20], thermomechanical surfaces [21] and surfaces with diffusion [6]. Motivated by Figures 1 and 2, we adopt the concept of surface energies to model differential growth of a thin film of epidermal cells, kinematically constrained to move with the parenchyma bulk, but allowed to grow at a different rate.

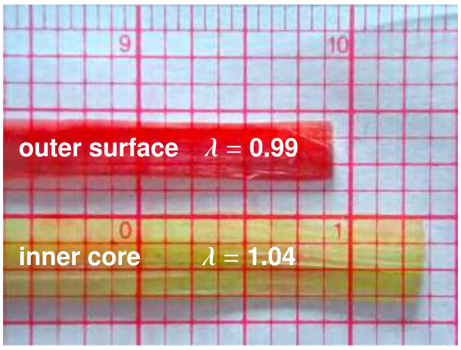

Figure 4: Peel test for model calibration. The red epidermal surface grows slower than the green parenchymal core. When the outer surface layer is peeled off the inner core, the epidermal surface contracts by ~ 1%, i.e., its stretch is $\lambda = 0.99$, while the parenchymal core expands by ~ 4%, i.e., its stretch is $\lambda = 1.04$. The peel test can serve to calibrate the relative surface growth to $\widehat{\vartheta} = 0.99/1.04 = 0.952$.

Characterizing differential growth experimentally is a challenging task. The classic opening angle experiment is probably the most established setup to quantify differential growth of living structures ex vivo [28]. While new methods have been proposed to characterize tissue growth in vivo [52], these approaches typically introduce the growth tensor as the gradient of a displacement field, implying that growth is a compatible process [38]. In their classical textbooks, plant physiologists suggest two conceptually simple experiments to visualize differential growth in plants: the peel test to quantify changes in length upon layer separation [1] and the longitudinal cutting test to quantify changes in curvature upon release of residual stress [10]. The petiole of rhubarb is an excellent model system for these two experiments, since its epidermal surface layer is easily distinguishable by its bright red color from the green bulk of the parenchyma ground substance. Figure 4 illustrates the classic peel test to quantify growth-induced changes in length. When the outer surface layer is peeled off the inner core, it contracts by approximately 1% generating a stretch of $\lambda = 0.99$, while the inner core expands by approximately 4% corresponding to a stretch of $\lambda = 1.04$. The peel test can serve as an easily reproducible experiment to calibrate the model and to identify the surface-to-volume growth ratio. Here, the surface-to-volume growth ratio is $0.99 : 1.04 = 0.952$. In the sequel, we systematically vary the surface-to-volume growth ratio and explore its impact on tissue form and function.

This manuscript is organized as follows. In Section 2, we introduce the kinematic equations, the balance equations, and the constitutive equations of finite surface growth. In each subsection, we independently discuss the equations for the inner bulk and for the outer surface. In Section 3, we derive the weak forms of these equations and discretize them in space using a combination of solid elements for the bulk and membrane elements for the surface. In Section 4, we demonstrate the features of growing surfaces using the model problem of growth-induced longitudinal tissue tension in a stalk of rhubarb. We close with a critical discussion in Section 5.

2. Governing equations

2.1. Kinematics

To model growing surfaces, we kinematically characterize the motion of material particles $\boldsymbol{X} \in \mathcal{B}_0$, where $\mathcal{B}_0 \subset \mathbb{R}^3$ denotes the material placement of a continuum body with a smooth surface $\mathcal{S}_0 = \partial\mathcal{B}_0$ in the reference configuration. We label points on the surface $\mathcal{S}_0$ as $\widehat{\boldsymbol{X}} = \boldsymbol{X}|_{\mathcal{S}_0}$ and

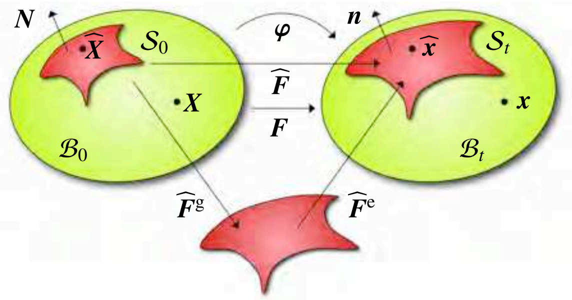

Figure 5: Kinematics of material and spatial configurations $\mathcal{B}_0$ and $\mathcal{B}_t$ of material body with material and spatial surfaces $\mathcal{S}_0$ and $\mathcal{S}_t$ and multiplicative decomposition of the surface deformation gradient $\widehat{\boldsymbol{F}} = \widehat{\boldsymbol{F}}^{\mathrm{e}} \cdot \widehat{\boldsymbol{F}}^{\mathrm{g}}$ into elastic part $\widehat{\boldsymbol{F}}^{\mathrm{e}}$ and growth part $\widehat{\boldsymbol{F}}^{\mathrm{g}}$.

denote the unit outward normal to $\mathcal{S}_0$ as $\boldsymbol{N}$, see Figure 5. We characterize the smooth motion of the material placement $\boldsymbol{X}$ onto its spatial placement $\boldsymbol{x}$ during the the time interval of interest $\mathbb{T} = [\,0, T\,] \subset \mathbb{R}^+$ through the volume deformation map $\boldsymbol{\varphi} : \mathcal{B}_0 \times \mathbb{T} \to \mathbb{R}^3$. Similarly, we characterize the motion of the corresponding surface placement $\widehat{\boldsymbol{X}}$ onto $\widehat{\boldsymbol{x}} = \boldsymbol{x}|_{\mathcal{S}_t}$ through the surface deformation map $\widehat{\boldsymbol{\varphi}} : \mathcal{S}_0 \times \mathbb{T} \to \mathbb{R}^3$,

$$\boldsymbol{x} = \boldsymbol{\varphi}\,(\boldsymbol{X}, t) \qquad \text{and} \qquad \widehat{\boldsymbol{x}} = \widehat{\boldsymbol{\varphi}}\,(\widehat{\boldsymbol{X}}, t)\,. \tag{1}$$

As indicated in Figure 5, we label the current placement of the body at time t as $\mathcal{B}_t = \boldsymbol{\varphi}\,(\mathcal{B}_0)$ and the associated surface as $\mathcal{S}_t = \boldsymbol{\varphi}\,(\mathcal{S}_0)$. That latter definition implies the concept of kinematic slavery, which requires that points on the surface of the body remain on the surface at all times. Next we introduce the volume deformation gradient $\boldsymbol{F}$, which maps material line elements $\mathrm{d}\boldsymbol{X}$ onto spatial line elements $\mathrm{d}\boldsymbol{x} = \boldsymbol{F} \cdot \mathrm{d}\boldsymbol{X}$ and the corresponding surface deformation gradient

$\widehat{\boldsymbol{F}}$, which maps tangential line elements from the material surface $\mathrm{d}\widehat{\boldsymbol{X}}$ onto the spatial surface $\mathrm{d}\widehat{\boldsymbol{x}} = \widehat{\boldsymbol{F}} \cdot \mathrm{d}\widehat{\boldsymbol{X}}$,

$$\boldsymbol{F} = \nabla\boldsymbol{\varphi} \qquad \text{and} \qquad \widehat{\boldsymbol{F}} = \widehat{\nabla}\widehat{\boldsymbol{\varphi}} = \boldsymbol{F} \cdot \widehat{\boldsymbol{I}}\,. \tag{2}$$

The volume gradient $\nabla\{\circ\} = \partial_{\boldsymbol{X}}\{\circ\}|_t$ follows from its standard definition, where $\{\circ\}|_t$ denotes a fixed position in time. The surface gradient $\widehat{\nabla}\{\circ\} = \nabla\{\circ\} \cdot \widehat{\boldsymbol{I}}$ follows from the projection of the volume gradient using the second order surface unit tensor $\widehat{\boldsymbol{I}} = \boldsymbol{I} - \boldsymbol{N} \otimes \boldsymbol{N}$. Here $\boldsymbol{I}$ is the classical second order unit tensor and $\boldsymbol{N}$ is the outward surface normal. The volume Jacobian J of the deformation gradient $\boldsymbol{F}$ relates material volume elements $\mathrm{d}V_0$ to spatial volume elements $\mathrm{d}V_t = J\,\mathrm{d}V_0$. Similarly, the surface Jacobian $\widehat{J}$ of the deformation gradient $\widehat{\boldsymbol{F}}$ relates material surface area elements $\mathrm{d}A_0$ to spatial surface area elements $\mathrm{d}A_t = \widehat{J}\,\mathrm{d}A_0$,

$$J = \det(\boldsymbol{F}) > 0 \qquad \text{and} \qquad \widehat{J} = \widehat{\det}(\widehat{\boldsymbol{F}}) = ||\, J\,\boldsymbol{F}^{-\mathrm{t}} \cdot \boldsymbol{N}\, || > 0\,. \tag{3}$$

Here, equation (3.2) is simply a form of Nanson's formua for the evolution of surface elements. To characterize surface growth, we multiplicatively decompose the surface deformation gradient $\widehat{\boldsymbol{F}}$ into an elastic part $\widehat{\boldsymbol{F}}^{\mathrm{e}}$ and a growth part $\widehat{\boldsymbol{F}}^{\mathrm{g}}$,

$$\widehat{\boldsymbol{F}} = \widehat{\boldsymbol{F}}^{\mathrm{e}} \cdot \widehat{\boldsymbol{F}}^{\mathrm{g}}\,. \tag{4}$$

Similarly, we multiplicatively decompose the surface Jacobian $\widehat{J}$ into an elastic part $\widehat{J}^{\mathrm{e}}$ and a growth part $\widehat{J}^{\mathrm{g}}$,

$$\widehat{J} = \widehat{J}^{\mathrm{e}}\,\widehat{J}^{\mathrm{g}} \qquad \text{with} \qquad \widehat{J}^{\mathrm{g}} = \widehat{\det}(\widehat{\boldsymbol{F}}^{\mathrm{g}}) = \frac{||[\,\widehat{\boldsymbol{F}}^{\mathrm{g}} \cdot \boldsymbol{A}_1\,] \times [\,\widehat{\boldsymbol{F}}^{\mathrm{g}} \cdot \boldsymbol{A}_2\,]||}{||\boldsymbol{A}_1 \times \boldsymbol{A}_2||}\,, \tag{5}$$

where $\widehat{J}^{\mathrm{g}}$ is defined in terms of the covariant base vectors $\boldsymbol{A}_1$ and $\boldsymbol{A}_2$ on the material surface $T\mathcal{S}_0$ [17].

Remark 1. *The second order surface unit tensor* $\widehat{\boldsymbol{I}}$ *serves as projection tensor to map the volume deformation gradient onto its surface counterpart,*

$$\widehat{\boldsymbol{F}} = \boldsymbol{F} \cdot \widehat{\boldsymbol{I}} \qquad \textit{with} \qquad \widehat{\boldsymbol{I}} = \boldsymbol{I} - \boldsymbol{N} \otimes \boldsymbol{N}\,, \tag{6}$$

where $\boldsymbol{N}$ *is the unit outward normal to the material surface* $\mathcal{S}_0$*. Since* $\widehat{\boldsymbol{I}}$ *is rank deficient, the surface deformation gradient* $\widehat{\boldsymbol{F}}$ *is typically non-invertible. However, it possesses a generalized inverse according to the following singular value decomposition,*

$$\widehat{\boldsymbol{F}}^{-1} \cdot \widehat{\boldsymbol{F}} = \widehat{\boldsymbol{I}} \qquad \widehat{\boldsymbol{F}} = \boldsymbol{U} \cdot \boldsymbol{\Sigma} \cdot \boldsymbol{V}^{\mathrm{t}} \qquad \widehat{\boldsymbol{F}}^{-1} = \boldsymbol{V} \cdot [\boldsymbol{\Sigma}^{+}]^{-1} \cdot \boldsymbol{U}^{\mathrm{t}} \tag{7}$$

where the diagonal entries of $\boldsymbol{\Sigma}$ *correspond to the singular values of* $\widehat{\boldsymbol{F}}$*, the columns of* $\boldsymbol{U}$ *and* $\boldsymbol{V}$ *are the left- and right-singular vectors associated with these singular values, and* $\boldsymbol{\Sigma}^{+}$ *is the pseudoinverse of* $\boldsymbol{\Sigma}$*, which is formed by replacing every non-zero diagonal entry by its reciprocal value.*

2.2. Balance equations

We introduce two balance equations of linear momentum, one for the volume and one for the surface. They balance the rate of change of the linear momentum, which we assume to vanish here for the quasi-static case considered here, with the divergence of the volume stresses $\boldsymbol{P}$ and forces $\boldsymbol{b}$ and, similarly, with the divergence of the surface stresses $\widehat{\boldsymbol{P}}$ and tractions $\widehat{\boldsymbol{b}} - \boldsymbol{P} \cdot \boldsymbol{N}$,

$$\boldsymbol{0} = \mathrm{Div}\,\boldsymbol{P} + \boldsymbol{b} \qquad \text{and} \qquad \boldsymbol{0} = \widehat{\mathrm{Div}}\,\widehat{\boldsymbol{P}} + [\,\widehat{\boldsymbol{b}} - \boldsymbol{P} \cdot \boldsymbol{N}]\,. \tag{8}$$

Here, $\mathrm{Div}\{\circ\} = \nabla\{\circ\} : \boldsymbol{I}$ and $\widehat{\mathrm{Div}}\{\circ\} = \widehat{\nabla}\{\circ\} : \widehat{\boldsymbol{I}}$ denote the volume and surface divergence operators. The volume stresses and forces $\boldsymbol{P}$ and $\boldsymbol{b}$ have the dimensions of force per unit area and force per unit volume, while the surface stresses and tractions $\widehat{\boldsymbol{P}}$ and $\widehat{\boldsymbol{b}} - \boldsymbol{P} \cdot \boldsymbol{N}$ have the dimensions of force per unit length and force per unit area. The surface tractions consist of two contributions, the prescribed surface tractions $\widehat{\boldsymbol{b}}$ and the surface tractions imposed by the underlying volume through the projected volume Piola stress $\boldsymbol{P} \cdot \boldsymbol{N}$ [47]. To obtain the weak forms of the balance of linear momentum, we multiply equations (8) with the test function $\delta\boldsymbol{\varphi}$, integrate them over the volume $\mathcal{B}_0$ and over the surface $\mathcal{S}_0$, and integrate them by parts.

$$\begin{aligned} \int_{\mathcal{B}_0} \nabla\delta\boldsymbol{\varphi} : \boldsymbol{P}\,\mathrm{d}V_0 \;&=\; \int_{\mathcal{B}_0} \delta\boldsymbol{\varphi} \cdot \boldsymbol{b}\,\mathrm{d}V_0 \;+\; \int_{\mathcal{S}_0} \delta\boldsymbol{\varphi} \cdot \boldsymbol{P} \cdot \boldsymbol{N}\,\mathrm{d}A_0 \\ \int_{\mathcal{S}_0} \widehat{\nabla}\delta\boldsymbol{\varphi} : \widehat{\boldsymbol{P}}\,\mathrm{d}A_0 \;&=\; \int_{\mathcal{S}_0} \delta\boldsymbol{\varphi} \cdot \widehat{\boldsymbol{b}}\,\mathrm{d}A_0 \;-\; \int_{\mathcal{S}_0} \delta\boldsymbol{\varphi} \cdot \boldsymbol{P} \cdot \boldsymbol{N}\,\mathrm{d}A_0 \;+\; \int_{\mathcal{C}_0} \delta\boldsymbol{\varphi} \cdot \widehat{\boldsymbol{P}} \cdot \boldsymbol{N}\,\mathrm{d}L_0\,. \end{aligned} \tag{9}$$

The volume equation (9.1) balances the internal volume forces with the external volume and surface forces. The surface equation (9.2) balances the internal surface forces with the external surface forces, the projected forces imposed by the underlying volume, and the external line forces along the boundary curve $\mathcal{C}_0$ of the surface $\mathcal{S}_0$.

2.3. *Constitutive equations*

To characterize the hyperelastic response of the volume, we introduce the free energy ψ, parameterized in terms of the volume deformation gradient $\boldsymbol{F}$. To characterize surface growth, we introduce an independent surface free energy $\widehat{\psi}$, parameterized in terms of the surface deformation gradient $\widehat{\boldsymbol{F}}$ and the surface growth tensor $\widehat{\boldsymbol{F}}^{\mathrm{g}}$, or, alternatively, in terms of the surface elastic tensor $\widehat{\boldsymbol{F}}^{\mathrm{e}} = \widehat{\boldsymbol{F}} \cdot \widehat{\boldsymbol{F}}^{\mathrm{g}-1}$,

$$\psi = \psi(\boldsymbol{F}) \qquad \text{and} \qquad \widehat{\psi} = \widehat{\psi}(\widehat{\boldsymbol{F}}, \widehat{\boldsymbol{F}}^{\mathrm{g}}) = \widehat{\psi}(\widehat{\boldsymbol{F}}^{\mathrm{e}})\,. \tag{10}$$

The volume and surface Piola stresses $\boldsymbol{P}$ and $\widehat{\boldsymbol{P}}$ follow from thermodynamic considerations as stress measures conjugate to the volume and surface deformation gradients $\boldsymbol{F}$ and $\widehat{\boldsymbol{F}}$,

$$\boldsymbol{P} = \frac{\partial\psi}{\partial\boldsymbol{F}} \quad \text{and} \quad \widehat{\boldsymbol{P}} = \frac{\partial\widehat{\psi}}{\partial\widehat{\boldsymbol{F}}} = \frac{\partial\widehat{\psi}}{\partial\widehat{\boldsymbol{F}}^{\mathrm{e}}} : \frac{\partial\widehat{\boldsymbol{F}}^{\mathrm{e}}}{\partial\widehat{\boldsymbol{F}}} = \widehat{\boldsymbol{P}}^{\mathrm{e}} \cdot \widehat{\boldsymbol{F}}^{\mathrm{g}\,-\,\mathrm{t}} \quad \text{with} \quad \widehat{\boldsymbol{P}}^{\mathrm{e}} = \frac{\partial\widehat{\psi}}{\partial\widehat{\boldsymbol{F}}^{\mathrm{e}}}\,, \tag{11}$$

where $\widehat{\boldsymbol{P}}^{\mathrm{e}}$ denotes the elastic surface stress. The total derivatives of the volume and surface stresses $\boldsymbol{P}$ and $\widehat{\boldsymbol{P}}$ with respect to the deformation gradients $\boldsymbol{F}$ and $\widehat{\boldsymbol{F}}$ introduce the fourth order volume and surface tangent moduli $\mathbb{A}$ and $\widehat{\mathbb{A}}$,

$$\mathbb{A} = \frac{\mathrm{d}\boldsymbol{P}}{\mathrm{d}\boldsymbol{F}} \quad \text{and} \quad \widehat{\mathbb{A}} = \frac{\mathrm{d}\widehat{\boldsymbol{P}}}{\mathrm{d}\widehat{\boldsymbol{F}}} = \frac{\mathrm{d}\widehat{\boldsymbol{P}}}{\mathrm{d}\widehat{\boldsymbol{F}}^{\mathrm{e}}} : \frac{\mathrm{d}\widehat{\boldsymbol{F}}^{\mathrm{e}}}{\mathrm{d}\widehat{\boldsymbol{F}}} = \widehat{\mathbb{A}}^{\mathrm{e}} : [\widehat{\boldsymbol{F}}^{\mathrm{g}\,-\,\mathrm{t}} \overline{\otimes} \widehat{\boldsymbol{F}}^{\mathrm{g}\,-\,\mathrm{t}}] \quad \text{with} \quad \widehat{\mathbb{A}}^{\mathrm{e}} = \frac{\mathrm{d}\widehat{\boldsymbol{P}}^{\mathrm{e}}}{\mathrm{d}\widehat{\boldsymbol{F}}} \tag{12}$$

where $\widehat{\mathbb{A}}^{\mathrm{e}}$ denotes the elastic surface tangent moduli. These tangent moduli will prove critical to guarantee optimal convergence of the algorithmic Newton-Raphson procedure.

2.4. *Growth*

To characterize growth, we prescribe the functional form of the growth tensor and its evolution in time. We consider the two simplest possible cases, isotropic and transversely isotropic surface growth, for which the surface growth tensors $\widehat{\boldsymbol{F}}^{\mathrm{g}}_{\mathrm{iso}}$ and $\widehat{\boldsymbol{F}}^{\mathrm{g}}_{\mathrm{trs}}$ can be parameterized in terms of a single scalar-valued growth multiplier $\widehat{\vartheta}$,

$$\widehat{\boldsymbol{F}}^{\mathrm{g}}_{\mathrm{iso}} = \widehat{\vartheta}\,\widehat{\boldsymbol{I}} \qquad \text{and} \qquad \widehat{\boldsymbol{F}}^{\mathrm{g}}_{\mathrm{trs}} = \widehat{\boldsymbol{I}} + [\widehat{\vartheta} - 1]\,\widehat{\boldsymbol{M}} \otimes \widehat{\boldsymbol{M}}\,. \tag{13}$$

Here, the surface unit vector $\widehat{\boldsymbol{M}}$ defines the direction of growth for the transversely isotropic case. We can quantify the amount of surface growth through the Jacobians,

$$\widehat{J}^{\mathrm{g}}_{\mathrm{iso}} = \widehat{\vartheta}^{2} \qquad \text{and} \qquad \widehat{J}^{\mathrm{g}}_{\mathrm{trs}} = \widehat{\vartheta}\,, \tag{14}$$

such that $\widehat{\vartheta} = 1$ characterizes the initial ungrown state, $\widehat{\vartheta} > 1$ indicates surface growth, and $\widehat{\vartheta} < 1$ indicates surface shrinkage. We suggest a simple exponential evolution equation for the growth multiplier,

$$\mathrm{D}_t\widehat{\vartheta} = [\,\widehat{\vartheta}_\infty - \widehat{\vartheta}_0\,]\,[\,\exp\left(-t/\widehat{\tau}\right)\,]\,/\,\widehat{\tau}\,, \tag{15}$$

where D_t denotes the material time derivative, $\widehat{\tau}$ characterizes the velocity of surface growth, $\widehat{\vartheta}_0 = 1.0$ is the initial growth value, and $\widehat{\vartheta}_\infty$ limits the final amount of surface growth towards which the growth multiplier $\widehat{\vartheta}$ converges as time increases. Because of its simple form, we can integrate the above equation explicitly,

$$\widehat{\vartheta}(t) = \widehat{\vartheta}_\infty + [\,\widehat{\vartheta}_0 - \widehat{\vartheta}_\infty\,]\,\exp\left(-t/\widehat{\tau}\right), \tag{16}$$

to directly identify the amount of growth $\widehat{\vartheta}$ at any given point in time t.

3. Discretization

Since surface growth is typically a highly nonlinear and possibly heterogeneous process, we suggest to solve its governing equations computationally within an incremental iterative nonlinear finite element scheme. We begin by summarizing the weak forms of the balance of linear momentum in the volume and on the surface (9),

$$\int_{\mathcal{B}_0} \nabla\delta\boldsymbol{\varphi} : \boldsymbol{P}\,\mathrm{d}V_0 - \int_{\mathcal{B}_0} \delta\boldsymbol{\varphi}\cdot\boldsymbol{b}\,\mathrm{d}V_0 + \int_{\mathcal{S}_0} \widehat{\nabla}\delta\boldsymbol{\varphi} : \widehat{\boldsymbol{P}}\,\mathrm{d}A_0 - \int_{\mathcal{S}_0} \delta\boldsymbol{\varphi}\cdot\widehat{\boldsymbol{b}}\,\mathrm{d}A_0 - \int_{\mathcal{C}_0} \delta\boldsymbol{\varphi}\cdot\widehat{\boldsymbol{P}}\cdot\boldsymbol{N}\,\mathrm{d}L_0 \doteq 0\,. \tag{17}$$

To discretize the weak form in space, we partition the domain of interest $\mathcal{B}_0 = \mathbf{U}_{\mathrm{e}=1}^{\mathrm{n_{be}}}\mathcal{B}_0^{\mathrm{e}}$ into $\mathrm{n_{be}}$ finite volume elements $\mathcal{B}_0^{\mathrm{e}}$, and the surface of interest $\mathcal{S}_0 = \mathbf{U}_{\mathrm{e}=1}^{\mathrm{n_{se}}}\mathcal{S}_0^{\mathrm{e}}$ into $\mathrm{n_{se}}$ finite surface elements $\mathcal{S}_0^{\mathrm{e}}$. Each surface element shares its nodes with its corresponding volume element as illustrated in Figure 7. This implies that the surface element acts like a shell element, which moves in consistency with the bulk, however, it is equipped with its own independent free energy function. To approximate the test functions $\delta\boldsymbol{\varphi}$, trial functions $\boldsymbol{\varphi}$, and nodal coordinates $\boldsymbol{X}$ in

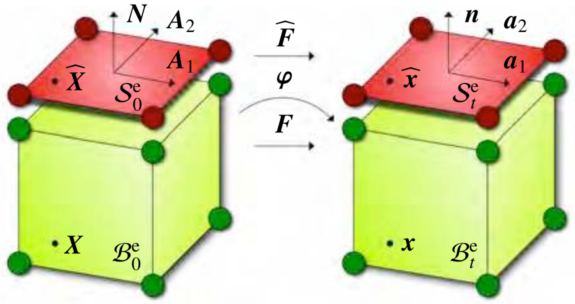

Figure 6: Discretization of material body with finite volume elements $\mathcal{B}_0^{\mathrm{e}}$ and $\mathcal{B}_t^{\mathrm{e}}$ and of its surface with finite surface elements $\mathcal{S}_0^{\mathrm{e}}$ and $\mathcal{S}_t^{\mathrm{e}}$. Surface elements share their nodes with the corresponding volume elements, however, they are equipped with their own energies $\widehat{\psi}$, stresses $\widehat{\boldsymbol{P}} = \partial\widehat{\psi}/\partial\widehat{\boldsymbol{F}}$, and tangent operators $\widehat{\mathbb{A}} = \mathrm{d}\widehat{\boldsymbol{P}}/\mathrm{d}\widehat{\boldsymbol{F}}$.

the volume and on the surface, we apply an isoparametric Bubnov-Galerkin type finite element interpolation,

$$\begin{aligned} \delta\boldsymbol{\varphi} &= \textstyle\sum_{i=1}^{\mathrm{n_{vn}}} N^i \,\delta\boldsymbol{\varphi}_i \quad &&\text{and} \quad \boldsymbol{\varphi} = \textstyle\sum_{j=1}^{\mathrm{n_{vn}}} N^j \,\boldsymbol{\varphi}_j \quad &&\text{and} \quad \boldsymbol{X} = \textstyle\sum_{i=1}^{\mathrm{n_{vn}}} N^i \,\boldsymbol{X}_i \\ \delta\boldsymbol{\varphi} &= \textstyle\sum_{i=1}^{\mathrm{n_{sn}}} \widehat{N}^i \,\delta\boldsymbol{\varphi}_i \quad &&\text{and} \quad \boldsymbol{\varphi} = \textstyle\sum_{j=1}^{\mathrm{n_{sn}}} \widehat{N}^j \,\boldsymbol{\varphi}_j \quad &&\text{and} \quad \boldsymbol{X} = \textstyle\sum_{i=1}^{\mathrm{n_{sn}}} \widehat{N}^i \,\boldsymbol{X}_i \,. \end{aligned} \tag{18}$$

Here $N^{i,j}$ and $\widehat{N}^{i,j}$ are the element shape functions in the volume and on the surface and $i, j = 1, .., \mathrm{n_{vn}}$ and $i, j = 1, .., \mathrm{n_{sn}}$ are the volume and surface nodes. The gradients of the test and trial functions in the volume and on the surface

$$\begin{aligned} \delta\boldsymbol{F} &= \nabla\delta\boldsymbol{\varphi} = \textstyle\sum_{i=1}^{\mathrm{n_{vn}}} \,\delta\boldsymbol{\varphi}_i \otimes \nabla N^i \quad &&\text{and} \quad \boldsymbol{F} = \nabla\boldsymbol{\varphi} = \textstyle\sum_{j=1}^{\mathrm{n_{vn}}} \,\boldsymbol{\varphi}_j \otimes \nabla N^j \\ \delta\boldsymbol{F} &= \widehat{\nabla}\delta\boldsymbol{\varphi} = \textstyle\sum_{i=1}^{\mathrm{n_{sn}}} \,\delta\boldsymbol{\varphi}_i \otimes \widehat{\nabla} N^i \quad &&\text{and} \quad \boldsymbol{F} = \widehat{\nabla}\boldsymbol{\varphi} = \textstyle\sum_{j=1}^{\mathrm{n_{sn}}} \,\boldsymbol{\varphi}_j \otimes \widehat{\nabla} N^j \end{aligned} \tag{19}$$

then follow naturally in terms of the gradients of the volume and surface shape functions

$$\begin{aligned} \nabla N^i &= \frac{\mathrm{d}N^i(\boldsymbol{\xi})}{\mathrm{d}\boldsymbol{X}} = \mathbf{J}^{-\mathrm{t}} \cdot \frac{\mathrm{d}N^i(\boldsymbol{\xi})}{\mathrm{d}\boldsymbol{\xi}} \quad \text{with} \quad \mathbf{J} = \frac{\mathrm{d}\boldsymbol{X}}{\mathrm{d}\boldsymbol{\xi}} \qquad\qquad\qquad\quad &&\text{and} \quad \boldsymbol{X} \;= \textstyle\sum_{i=1}^{\mathrm{n_{vn}}} N^i(\boldsymbol{\xi})\boldsymbol{X}_i \\ \widehat{\nabla} N^i &= \frac{\mathrm{d}\widehat{N}^i(\boldsymbol{\xi})}{\mathrm{d}\boldsymbol{X}} = \widehat{\mathbf{J}}^{-\mathrm{t}} \cdot \frac{\mathrm{d}\widehat{N}^i(\boldsymbol{\xi})}{\mathrm{d}\boldsymbol{\xi}} \quad \text{with} \quad \widehat{\mathbf{J}} = \frac{\mathrm{d}\boldsymbol{X}}{\mathrm{d}\boldsymbol{\xi}} = [\boldsymbol{A}_1, \boldsymbol{A}_2] \quad &&\text{and} \quad \boldsymbol{A}_\alpha = \textstyle\sum_{i=1}^{\mathrm{n_{sn}}} \boldsymbol{X}_i \, \widehat{N}^i_{,\xi\alpha} \,. \end{aligned} \tag{20}$$

Herein $\boldsymbol{A}_\alpha$ for $\alpha = 1, 2$ are the contravariant material base vectors. With these discretizations, equation (17) transforms into the following discrete residual

$$\mathbf{R}_I = \overset{\mathrm{n_{el}}}{\underset{\mathrm{e}=1}{\mathbf{A}}} \int_{\mathcal{B}_0^{\mathrm{e}}} \nabla N^i \cdot \boldsymbol{P} \,\mathrm{d}V_{\mathrm{e}} - \int_{\mathcal{B}_0^{\mathrm{e}}} N^i \,\boldsymbol{b} \,\mathrm{d}V_{\mathrm{e}} + \int_{\mathcal{S}_0^{\mathrm{e}}} \widehat{\nabla} N^i \cdot \widehat{\boldsymbol{P}} \,\mathrm{d}A_{\mathrm{e}} - \int_{\mathcal{S}_0^{\mathrm{e}}} \widehat{N}^i \,\widehat{\boldsymbol{b}} \,\mathrm{d}A_{\mathrm{e}} - \int_{\mathcal{C}_0^{\mathrm{e}}} \widehat{N}^i \,\widehat{\boldsymbol{P}} \cdot \boldsymbol{N} \,\mathrm{d}L_{\mathrm{e}} \doteq \boldsymbol{0} \,, \tag{21}$$

where the operator $\mathbf{A}$ symbolizes the assembly of all element residuals at the $i = 1, .., \mathrm{n_{vn}}$ element nodes to the global residual at the global node points $I = 1, .., \mathrm{n_{gn}}$. To solve the above equation, we use an incremental iterative Newton-Raphson algorithm based on the consistent linearization of the residual $\mathbf{R}_I$ with respect to the nodal vector of unknowns $\boldsymbol{\varphi}_J$. This linearization introduces the global stiffness matrix $\mathbf{K}_{IJ}$ at all global nodes $I, J = 1, .., \mathrm{n_{ng}}$,

$$\mathbf{K}_{IJ} = \frac{\mathrm{d}\mathbf{R}_I}{\mathrm{d}\boldsymbol{\varphi}_J} = \overset{\mathrm{n_{el}}}{\underset{\mathrm{e}=1}{\mathbf{A}}} \int_{\mathcal{B}_0^{\mathrm{e}}} [\,\boldsymbol{I} \cdot \nabla N^i\,] : \mathbb{A} \cdot \nabla N^j \,\mathrm{d}V_{\mathrm{e}} + \int_{\mathcal{S}_0^{\mathrm{e}}} [\,\widehat{\boldsymbol{I}} \cdot \widehat{\nabla} N^i\,] : \widehat{\mathbb{A}} \cdot \widehat{\nabla} N^j \,\mathrm{d}A_{\mathrm{e}} \,. \tag{22}$$

For each global Newton iteration step, we iteratively update the current deformation state $\boldsymbol{\varphi}_J \leftarrow \boldsymbol{\varphi}_J - \mathbf{K}_{IJ}^{-1} \cdot \mathbf{R}_I$ until we achieve algorithmic convergence. Upon convergence, we store the surface growth multipliers $\widehat{\vartheta}^{\mathrm{g}}$ at the integration points of the corresponding surface elements.

4. Results

We illustrate the performance of the proposed surface growth model by simulating differential growth in a stalk of rhubarb. Unless stated otherwise, we model the stalk as a cylindrical tube with a length of $l = 7.0$ cm and a radius of $r = 0.375$ cm. To visualize the effect of different surface-to-volume growth ratios, we virtually cut the stalk in fourths, fix it at one end, and allow its surface to shrink by gradually decreasing the surface growth multiplier $\widehat{\vartheta}$. We discretize one fourth of the inner parenchyma core with 32 elements along the length and 80 elements across the cross section. In each cross section, we discretize the corresponding epidermal surface with 8 additional surface elements around the circumference. This results in a discretization with 2,560 elastic eight-noded volume elements and 256 growing four-noded surface elements with a total of 3,201 nodes and 9,603 degrees of freedom. We characterize the hyperelastic responses of the volume and surface using independent isotropic Helmholtz energies ψ_0 and $\widehat{\psi}_0$ of Neo-Hookean type,

$$\begin{aligned} \psi_0 &= \tfrac{1}{2}\,\mu\,[\,\boldsymbol{F} \;:\, \boldsymbol{F} \;\; -3 - 2\ln J \;\;] + \tfrac{1}{2}\,\lambda\ln^2 J \\ \widehat{\psi}_0 &= \tfrac{1}{2}\,\widehat{\mu}\,[\,\widehat{\boldsymbol{F}}^{\mathrm{e}} : \widehat{\boldsymbol{F}}^{\mathrm{e}} -2 - 2\ln \widehat{J}^{\mathrm{e}}\,] + \tfrac{1}{2}\,\widehat{\lambda}\ln^2 \widehat{J}^{\mathrm{e}}\,. \end{aligned}$$

Here, λ and μ are the standard Lamé constants of the volume and $\widehat{\lambda}$, and $\widehat{\mu}$ are the Lamé constants of the surface. To evaluate the discrete residual (21), we calculate the volume and surface Piola stresses $\boldsymbol{P}$ and $\widehat{\boldsymbol{P}} = \widehat{\boldsymbol{P}}^{\mathrm{e}} \cdot \widehat{\boldsymbol{F}}^{\mathrm{g}\,-\,\mathrm{t}}$ using the general definitions (11),

$$\begin{aligned} \boldsymbol{P} \;\; &= \mu\,\boldsymbol{F} \;\; + [\,\lambda \ln J \;\; - \mu\,]\,\boldsymbol{F}^{-\mathrm{t}} \\ \widehat{\boldsymbol{P}}^{\mathrm{e}} &= \widehat{\mu}\,\widehat{\boldsymbol{F}}^{\mathrm{e}} + [\,\widehat{\lambda} \ln \widehat{J}^{\mathrm{e}} - \widehat{\mu}\,]\,\widehat{\boldsymbol{F}}^{\mathrm{e}\,-\,\mathrm{t}}\,. \end{aligned}$$

To evaluate the consistent algorithmic linearization of the residual (22), we calculate the volume and surface tangent moduli $\mathbb{A}$ and $\widehat{\mathbb{A}} = \widehat{\mathbb{A}^{\mathrm{e}}} : [\widehat{\boldsymbol{F}}^{\mathrm{g}\,-\,\mathrm{t}} \overline{\otimes} \widehat{\boldsymbol{F}}^{\mathrm{g}\,-\,\mathrm{t}}]$ using the general definitions (12),

$$\begin{aligned} \mathbb{A} \;\; &= \mu\,\boldsymbol{I}\,\overline{\otimes}\,\boldsymbol{I} + [\,\mu - \lambda \ln J \;\;]\; \boldsymbol{F}^{-\mathrm{t}} \underline{\otimes}\, \boldsymbol{F}^{-1} + \lambda\,\boldsymbol{F}^{-\mathrm{t}} \otimes \boldsymbol{F}^{-\mathrm{t}} \\ \widehat{\mathbb{A}}^{\mathrm{e}} &= \widehat{\mu}\,\boldsymbol{I}\,\overline{\otimes}\,\widehat{\boldsymbol{I}} + [\,\widehat{\mu} - \widehat{\lambda} \ln \widehat{J}^{\mathrm{e}}\,]\,[\,\widehat{\boldsymbol{F}}^{\mathrm{e}\,-\,\mathrm{t}} \underline{\otimes}\, \widehat{\boldsymbol{F}}^{\mathrm{e}\,-\,1} - \widehat{\boldsymbol{i}^{\perp}}\,\overline{\otimes}\,[\,\widehat{\boldsymbol{F}}^{\mathrm{e}\,-\,1} \cdot \widehat{\boldsymbol{F}}^{\mathrm{e}\,-\,\mathrm{t}}\,]\,] + \widehat{\lambda}\,\widehat{\boldsymbol{F}}^{\mathrm{e}\,-\,\mathrm{t}} \otimes \widehat{\boldsymbol{F}}^{\mathrm{e}\,-\,\mathrm{t}}\,, \end{aligned}$$

where we have introduced the abbreviation $\boldsymbol{i}^{\perp}$ for the spatial second order normal projection tensor $\boldsymbol{i}^{\perp} = \boldsymbol{F} \cdot \boldsymbol{N} \otimes \boldsymbol{F} \cdot \boldsymbol{N}$. To model the elastic response of the parenchyma core, we choose Lamé constants of $\lambda = 0.577$ N/mm^2 and $\mu = 0.385$ N/mm^2. While the epidermis in plants typically tends to be stiffer and stronger in than the bulk, here, for the sake of simplicity, we choose similar Lamé constants of $\widehat{\lambda} = 0.577$ N/mm^2 and $\widehat{\mu} = 0.385$ N/mm^2 for the epidermal surface. To model the difference in growth between the inner parenchyma core and the outer epidermal surface, we gradually decrease the surface growth multiplier $\widehat{\vartheta}$ by choosing an infinite

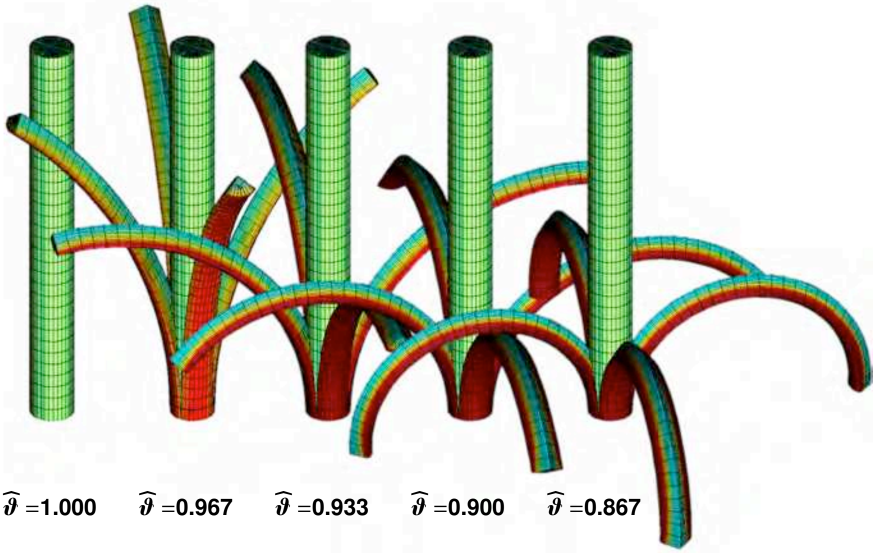
$\widehat{\vartheta}$ =1.000
$\widehat{\vartheta}$ =0.967
$\widehat{\vartheta}$ =0.933
$\widehat{\vartheta}$ =0.900
$\widehat{\vartheta}$ =0.867

Figure 7: Growth-induced longitudinal tissue tension in stalk of rhubarb. The stalk is modeled as a cylindrical tube with elastic volume elements and growing surface elements. With decreasing surface-to-volume growth ratios from $\widehat{\vartheta} = 1.000$, to $\widehat{\vartheta} = 0.967$, $\widehat{\vartheta} = 0.933$, $\widehat{\vartheta} = 0.900$, and $\widehat{\vartheta} = 0.867$, from left to right, the tissue tension increases and induces a higher curvature when the stalk is cut in fourths. Red colors indicate compression, green and blue colors indicate tension.

growth multiplier of $\widehat{\vartheta}_\infty = 0.5$, a time constant of $\widehat{\tau} = 1.0$, and an initial discrete time step size of $\Delta t = 0.1$. The choice of the latter two parameters, however, does not affect the results we present in the sequel.

Figure 7 illustrates the effect of growth-induced longitudinal tissue tension in the rhubarb stalk. The snap shots correspond to surface-to-volume growth ratios gradually decreasing from $\widehat{\vartheta} = 1.000$, to $\widehat{\vartheta} = 0.967$, $\widehat{\vartheta} = 0.933$, $\widehat{\vartheta} = 0.900$, and $\widehat{\vartheta} = 0.867$, from left to right. As the surface-to-volume growth ratio decreases, the tissue tension increases and induces a higher curvature when the stalk is cut in fourths. Since the outer epidermal surface shrinks with respect to the inner parenchyma core, the four sections of the stalk gradually bend outward. The colorcode indicates the growth-induced increase in tissue stress with red colors indicating tissue compression and green and blue colors indicating tissue tension.

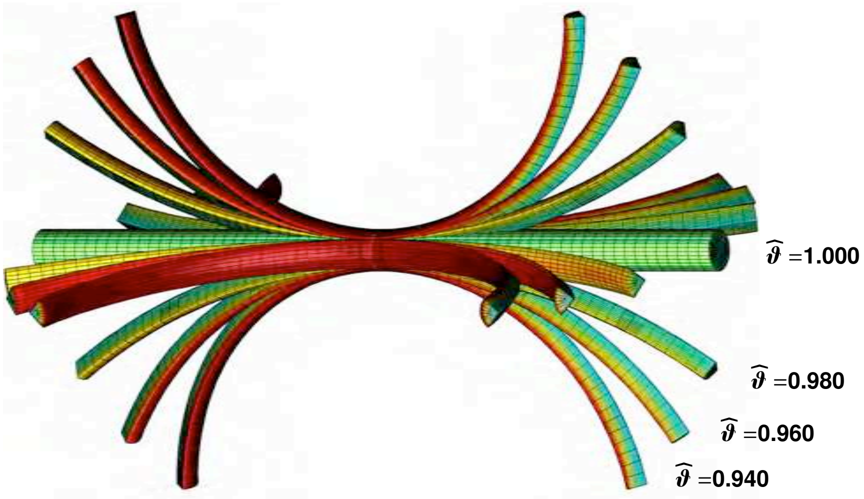
$\widehat{\vartheta}$ =1.000
$\widehat{\vartheta}$ =0.980
$\widehat{\vartheta}$ =0.960
$\widehat{\vartheta}$ =0.940

Figure 8: Growth-induced longitudinal tissue tension in stalk of rhubarb. The stalk is modeled as a cylindrical tube with elastic volume elements and growing surface elements. With decreasing surface-to-volume growth ratios from $\widehat{\vartheta} = 1.000$, to $\widehat{\vartheta} = 0.980$, $\widehat{\vartheta} = 0.960$, and $\widehat{\vartheta} = 0.940$, the surface tension increases and induces a higher curvature when the stalk is cut in fourths. Red colors indicate compression, green and blue colors indicate tension.

Figure 8 displays the effect of different surface-to-volume growth ratios overlaid in a single image. With decreasing surface-to-volume growth ratios from $\widehat{\vartheta} = 1.000$, to $\widehat{\vartheta} = 0.980$, $\widehat{\vartheta} = 0.960$, and $\widehat{\vartheta} = 0.940$, the surface tension increases and induces a higher curvature when the stalk is cut in four sections. Again, red colors indicate tissue compression, green and blue colors indicate tissue tension.

Figure 9 illustrates the effect of surface growth as the surface-to-volume growth ratio decreases gradually until the rhubarb stalk forms a closed loop. With decreasing surface-to-volume growth ratios from $\widehat{\vartheta} = 1.000$, to $\widehat{\vartheta} = 0.975$, $\widehat{\vartheta} = 0.950$, $\widehat{\vartheta} = 0.925$, $\widehat{\vartheta} = 0.900$, $\widehat{\vartheta} = 0.850$, and $\widehat{\vartheta} = 0.750$, the surface tension increases and induces a higher curvature when the stalk is cut in four sections. Again, red colors indicate tissue compression, green and blue colors indicate tissue tension.

Figure 10 quantifies the growth-induced curvature change in rhubarb stalks with different radius-to-length ratios. For this simulation, we decrease the mesh size to 16 elements along the length, 40 elements across the cross section, and 4 surface elements per cross section. This results in a discretization with 320 elastic eight-noded volume elements and 64 growing four-noded surface elements with a total of 493 nodes and 1,479 degrees of freedom. We keep the length of the stack constant at $l = 7.0\,\text{cm}$ and vary the radius from $r = 0.250\,\text{cm}$ to $r = 0.375\,\text{cm}$, $r = 0.500\,\text{cm}$, $r = 0.675\,\text{cm}$, and $r = 0.750\,\text{cm}$. A decrease in the surface-to-volume growth ratio $\widehat{\vartheta}$ increases

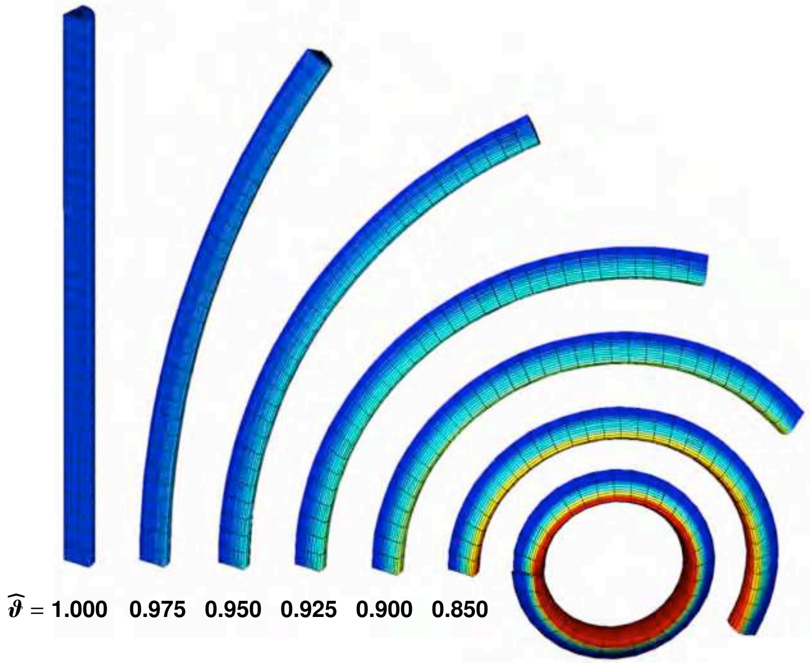

Figure 9: Growth-induced longitudinal tissue tension in stalk of rhubarb. The stalk is modeled as a quarter of a cylindrical tube with elastic volume elements and growing surface elements. With decreasing surface-to-volume growth ratios from $\widehat{\vartheta} = 1.000$, to $\widehat{\vartheta} = 0.975$, $\widehat{\vartheta} = 0.950$, $\widehat{\vartheta} = 0.925$, $\widehat{\vartheta} = 0.900$, $\widehat{\vartheta} = 0.850$, and $\widehat{\vartheta} = 0.750$, the surface tension increases and induces a higher curvature when the stalk is cut in fourths. Red colors indicate compression, green and blue colors indicate tension.

tissue tension. This induces an increase in relative curvature κ/κ_0 from $\kappa/\kappa_0 = 0.0$, corresponding to a straight line, to $\kappa/\kappa_0 = 1.0$, corresponding to a closed loop, where $\kappa_0 = 2\pi / l$. The surface-to-volume growth ratio $\widehat{\vartheta}$ required to form this closed loop decreases with increasing radius-to-length ratios, from $\widehat{\vartheta} = 0.894$, to $\widehat{\vartheta} = 0.887$, $\widehat{\vartheta} = 0.872$, $\widehat{\vartheta} = 0.853$, and $\widehat{\vartheta} = 0.838$, from blue to red lines. Upon isometric scaling, e.g., when doubling both, the stalk length l and radius r, the resulting curvature versus surface-to-volume growth curves remain identical as expected.

Figure 11 illustrates snapshots associated with the curves in Figure 10. In particular, the top row corresponds to the straight line at a relative curvature of $\kappa/\kappa_0 = 0.0$, while the bottom row corresponds to the formation of a closed loop at $\kappa/\kappa_0 = 1.0$ indicated through the solid dots in Figure 10. For the same curvature configuration, displayed in the individual rows, tissue stresses increase with increasing radius-to-length ratios, from left to right.

5. Discussion

Growth of thin surfaces plays a central role in the morphogenesis of many biological structures [55]. In plants, the differential growth of thin layers of cells is critical to establish structural form and function [1]. While the individual layers of a plant stem are relatively compliant when considered in plain isolation, differential growth creates a mechanical environment of residual stress that stiffens the structure as a whole [41]. Residual stresses can be generated by a fast growing inner core of parenchyma cells covered by a slowly growing thin layer of epidermal cells. By peeling off the thin surface layer, we can release residual stresses and observe a significant lengthening of the inner core, while the surface layer contracts as illustrated in Figure 1 [10].

Modeling differential growth of thin films can be conceptually challenging, especially because

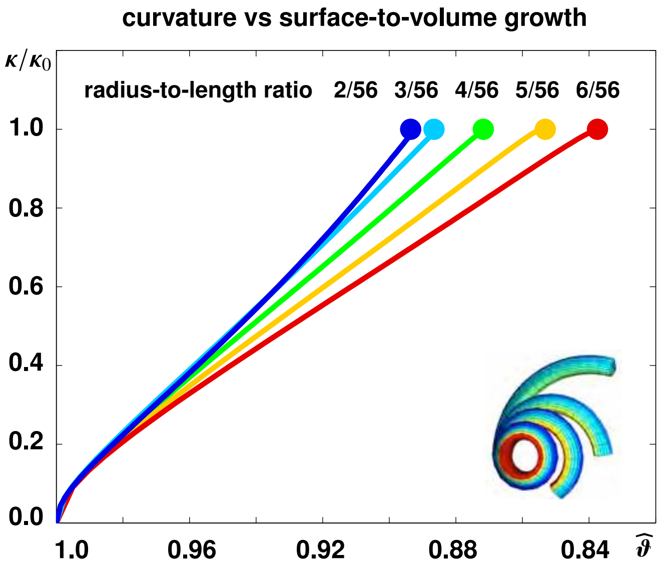

Figure 10: Growth-induced curvature changes in stalk of rhubarb for different radius-to-length ratios. A decrease in the surface-to-volume growth ratio $\widehat{\vartheta}$ increases tissue tension and induces an increase in relative curvature κ/κ_0. At a relative curvature of $\kappa/\kappa_0 = 1.0$, indicated throughout the solid dots, each stalk forms a closed loop. The surface-to-volume growth ratio $\widehat{\vartheta}$ required to form a closed loop, as shown in Figure 11, bottom row, decreases with increasing radius-to-length ratios, from $\widehat{\vartheta} = 0.894$, to $\widehat{\vartheta} = 0.887$, $\widehat{\vartheta} = 0.872$, $\widehat{\vartheta} = 0.853$, and $\widehat{\vartheta} = 0.838$, from blue to red.

most biological surfaces are typically only a few micrometers thick [53]. An elegant way to model growing thin biological layers is the concept of surface energies [16]. Introduced more than two centuries ago to characterize surface tension in droplets [24, 57], surface energies allow us to represent extremely thin surfaces as two-dimensional manifolds at the zero-thickness limit. This dimensional reduction is particularly valuable in the context of numerics, since the fully three-dimensional discretization of thin surfaces would either require very fine meshes, or generate numerically ill-conditioned systems [20]. To avoid these numerical difficulties, we simply equip the surface with its own free energy, which we allow to evolve independently of the bulk [45, 47]. In particular, our surface energy not only accounts for the elastic behavior of the surface itself, but also for its growth or shrinkage with respect to the bulk [36]. To kinematically characterize the amount of surface growth, we adopt the multiplicative decomposition of the surface deformation gradient into an elastic tensor and a growth tensor [59].

A conceptually elegant approach to experimentally characterize the surface growth tensor in plants is the classical peel test [10] as demonstrated in Figure 4. In this experiment, surface growth can simply be interpreted as the ratio between surface shortening and volume lengthening after both substructures are separated [1]. Virtually anybody can perform a simple peel test with rhubarb in their own kitchen, measure surface shortening and volume lengthening, and verify correct layer separation simply by the distinct red and green tissue colors [53]. Upon peeling several rhubarb stacks, we observed surface shortening of the order of -1% and the volume lengthening of the order of +4%. These values are slightly less pronounced than the surface shortening of -2-4% and the volume lengthening of +6% reported in the literature [54], most likely because our rhubarb stacks were not freshly harvested and their lower water content might play an important role.

An equally simple model experiment to quantify growth upon releasing tissue tension is the longitudinal cutting test [10]. When cutting the cylindrical plant stem in four equal parts, the epi-

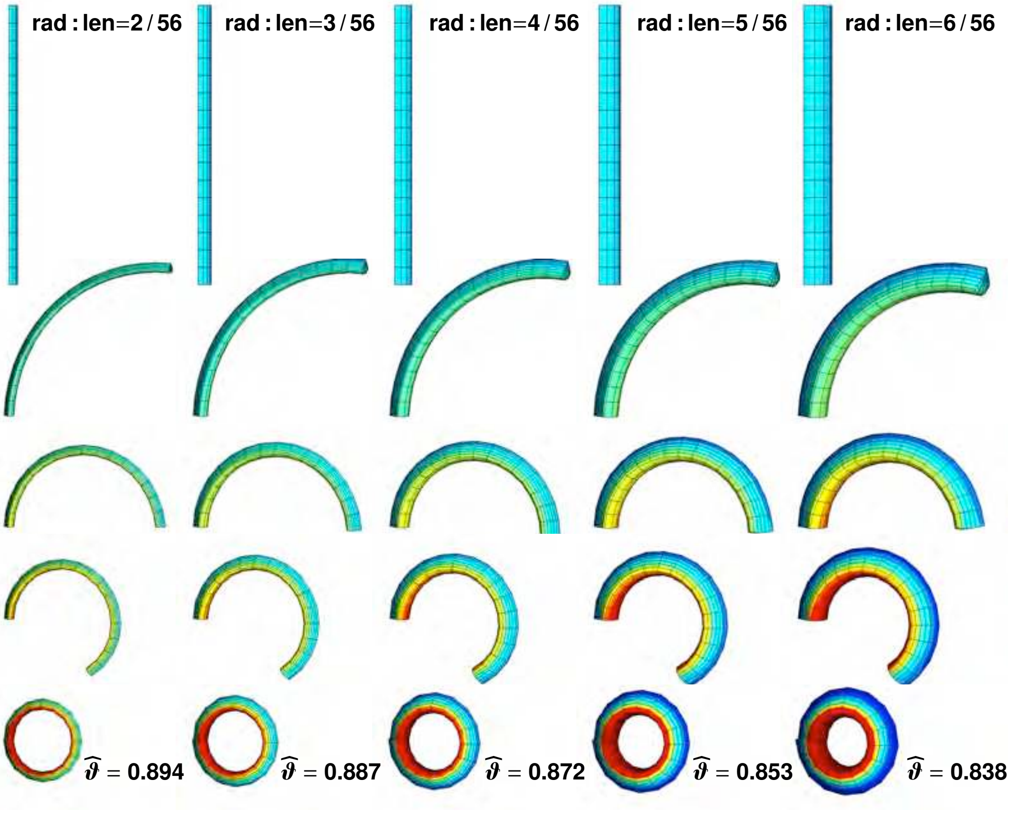
rad : len=2 / 56
rad : len=3 / 56
rad : len=4 / 56
rad : len=5 / 56
rad : len=6 / 56
$\widehat{\vartheta}$ = 0.894
$\widehat{\vartheta}$ = 0.887
$\widehat{\vartheta}$ = 0.872
$\widehat{\vartheta}$ = 0.853
$\widehat{\vartheta}$ = 0.838

Figure 11: Growth-induced curvature changes in stalk of rhubarb for different radius-to-length ratios. A decrease in the surface-to-volume growth ratio, from top to bottom, increases tissue tension and induces an increase in curvature. The top row corresponds to the straight stalk at a relative curvature of $\kappa/\kappa_0 = 0.0$, while the bottom row corresponds to the formation of a closed loop at $\kappa/\kappa_0 = 1.0$ indicated through the solid dots in Figure 10. The surface-to-volume growth ratio required to form a closed loop decreases with increasing radius-to-length ratios, from left to right. Red colors indicate compression, green and blue colors indicate tension.

dermal surface layers contract and bend outward, while the inner parenchyma core expands [1]. The release of tissue tension generates a state of bending, which we can quantify kinematically in terms of the stalk curvature [14]. Here, we have simulated the longitudinal cutting tests, and systematically varied the amount of surface growth and the radius-to-length ratio. Intuitively, as illustrated in Figure 10, the relative stalk curvature increases with increasing surface growth. For the same surface growth, thicker stems curve less upon longitudinal cutting than thinner stems. While the curvature is sensitive to both the amount surface growth the radius-to-length ratio, it is unaffected by isometric scaling: proportional changes in radius and length do not affect curvature and shape. Despite the large deformations associated with bending a straight line to a closed loop illustrated in Figures 9 and 11, our surface growth algorithm always performed stably and robustly, with no evidence of ill-conditioning or loss of convergence [36].

Our results demonstrate that the framework for continua with growing surfaces is an elegant setting to model growing thin biological films. Plant biology presents an illustrative area of application for growing surfaces, especially because the underlying experiments are simple, illustrative, and easily reproducible, even outside an advanced laboratory setting. Growing plants can serve as elegant model problems to calibrate surface growth models and validate computational algorithms. Beyond classical model problems in plant biology, our novel theoretical and computational framework for growing surfaces has immediate biomedical applications in asthma [33], gastritis [27], obstructive sleep apnoea [22], brain development [56], and tumor invasion [2]. It naturally captures the distinct mechanical behavior of a thin epidermal layer, which is typically only a few micrometers thick. Similar thin film phenomena are inherent to applications in material sciences, manufacturing, and microfabrication [26]. We believe that the proposed framework can provide insight into the complex interplay between thin films and the bulk, which might be particularly valuable when designing novel functionalized surfaces with distinct user-defined properties.

Acknowledgements

Maria A. Holland was supported by a Stanford Graduate Fellowship. Alain Goriely is a Wolfson Royal Society Merit Holder and acknowledges support from a Reintegration Grant under EC Framework VII and from award KUK-C1-013-04 by the King Abdullah University of Science and Technology KAUST. Ellen Kuhl acknowledges support by the National Science Foundation CAREER award CMMI 0952021 and INSPIRE grant 1233054 and by the National Institutes of Health grant U54 GM072970.

References

[1] Atkinson GF. Lessons in Botany. Henry Hold & Co, New York, 1900.

[2] Ambrosi D, Mollica F. On the mechanics of a growing tumor. *Int J Eng Sci*. 2002;40:1297-1316.

[3] Ambrosi D, Guana F. Stress modulated growth. *Math Mech Solids*. 2007;12:319-343.

[4] Ambrosi D, Ateshian GA, Arruda EM, Cowin SC, Dumais J, Goriely A, Holzapfel GA, Humphrey JD, Kemkemer R, Kuhl E, Olberding JE, Taber LA, Garikipati K. Perspectives on biological growth and remodeling. *J Mech Phys Solids*. 2011;59:863-883.

[5] Ben Amar M, Goriely A. Growth and instability in elastic tissues. *J Mech Phys Solids*. 2005;53:2284-2319.

[6] McBride AT, Javili A, Steinmann P, Bargmann S. Geometrically nonlinear continuum theories with surface energies coupled to diffusion. *J Mech Phys Solids.* 2011;59:2116-2133.

[7] Buganza Tepole A, Ploch CJ, Wong J, Gosain AK, Kuhl E. Growing skin - A computational model for skin expansion in reconstructive surgery. *J Mech Phys Solids*. 2011;59:2177-2190.

[8] Dorfmann A, Haughton DM. Stability and bifurcation of compressed elastic cylindrical tubes. *Int J Eng Sci.* 2006;44:1353-1365.

[9] Dorfmann A, Wilson C, Edgar ES, Peattie RA. Evaluating patient-specific abdominal aortic aneurysm wall stress based on flow-induced loading. *Biomech Model Mechanobio.* 2010;9:127-139.

[10] Gager CS. Fundamentals of Botany. P. Blakiston's Son & Co, Philadelphia, 1916.

[11] Garikipati K. The kinematics of biological growth. *Appl Mech Rev.* 2009;62:030801.1-030801.7.

[12] Göktepe S, Abilez OJ, Parker KK, Kuhl E. A multiscale model for eccentric and concentric cardiac growth through sarcomerogenesis. *J Theor Bio.* 2010;265:433-442.

[13] Göktepe S, Abilez OJ, Kuhl E. A generic approach towards finite growth with examples of athlete's heart, cardiac dilation, and cardiac wall thickening. *J Mech Phys Solids.* 2010;58:1661-1680.

[14] Goldstein RE, Goriely A. Dynamic buckling of morphoelastic filaments. *Phys Rev E.* 2006;74:010901.

[15] Goriely A, BenAmar M. Differential growth and instability in elastic shells. *Phys Rev Letters.* 2005;94:198103.

[16] Gurtin ME, Murdoch A. A continuum theory of elastic material surfaces. *Arch Rational Mech Anal.* 1975;57:291323.

[17] Gurtin ME, Struthers A. Multiphase thermomechanics with interfacial structure. *Arch Rational Mech Anal.* 1990;112:97160.

[18] Himpel G, Kuhl E, Menzel A, Steinmann P. Computational modeling of isotropic multiplicative growth. *Comp Mod Eng Sci.* 2005;8:119-134.

[19] Javili A, Steinmann P. A finite element framework for continua with boundary energies. Part I: The two-dimensional case. *Comp Meth Appl Mech Eng.* 2009;198:2198-2208.

[20] Javili A, Steinmann P. A finite element framework for continua with boundary energies. Part II: The three-dimensional case. *Comp Meth Appl Mech Eng.* 2010;199:755-765.

[21] Javili A, Steinmann P. A finite element framework for continua with boundary energies. Part III: The thermomechanical case. *Comp Meth Appl Mech Eng.* 2011;200:1963-1977.

[22] Kairaitis K. Pharyngeal wall fold influences on the collapsibility of the pharynx. *Med Hypotheses.* 2012;79:327-376.

[23] Kuhl E, Maas R, Himpel G, Menzel A. Computational modeling of arterial wall growth: Attempts towards patient-specific simulations based on computer tomography. *Biomech Mod Mechanobio.* 2007;6:321-331.

[24] Laplace PS. Traité de Mécanique Céleste. Oeuvres complète, Vol. 4, Suppl. 1, Livre X:771-777. 1805; Gauthier-Villars, Paris.

[25] Lee EH. Elastic-plastic deformation at finite strains. *J Appl Mech.* 1969;36:1-6.

[26] Li B, Cao YP, Feng XQ, Gao H. Mechanics of morphological instabilities and surface wrinkling in soft materials: A review. *Soft Matter.* 2012;8:5728-5745.

[27] Liao D, Zhao J, Gregersen H. The oesophageal zero-stress state and mucosal folding from a giome perspective. *World J Gastroenterol.* 2007;13:1347-1351.

[28] Liu SQ, Fung YC. Relationship between hypertension, hypertrophy, and opening angle of zero-stress state of arteries following aortic constriction. *J Biomech Eng.* 1989,111:325-335.

[29] McMahon J, Goriely A. Spontaneous cavitation in growing elastic membranes. *Math Mech Solids.* 2010;15:57-77.

[30] Menzel A. Modelling of anisotropic growth in biological tissues - A new approach and computational aspects. *Biomech Model Mechanobiol.* 2005;3:147-171.

[31] Menzel A, Kuhl E. Frontiers in growth and remodeling. *Mech Res Comm*. 2012;42,1-14.

[32] Moulton DE, Goriely A. Circumferential buckling instability of a growing cylindrical tube. *J Mech Phys Solids.* 2011;59:525-537.

[33] Moulton DE, Goriely A. Possible role of differential growth in airway wall remodeling in asthma. *J Appl Physiol.* 2011;110:1003-1012.

[34] Müller NJC. Handbuch der Botanik. Carl Winter's Universitätsbuchhandlung, Heidelberg, 1880.

[35] Nelson MR, Howard D, Jensen OE, King JR, Rose FRAJ, Waters SL. Growth-induced buckling of an epithelial layer. *Biomech Model Mechanobio.* 2011;10:883-900.

[36] Papastavrou A, Steinmann P, Kuhl E. On the mechanics of continua with boundary energies and growing surfaces. *J Mech Phys Solids.* 2013; accepted for publication.

[37] Rausch MK, Dam A, Göktepe S, Abilez OJ, Kuhl E. Computational modeling of growth: Systemic and pulmonary hypertension in the heart. *Biomech Model Mechanobiol.* 2011;10:799-811.

[38] Rausch MK, Tibayan FA, Miller DC, Kuhl E. Evidence of adaptive mitral leaflet growth. *J Mech Behavior Biomed Mat*. 2012;15:208-217.

[39] Rausch MK, Kuhl E. On the effect of prestrain and residual stress in thin biological membranes. *submitted for publication.* 2013.

[40] Rodriguez EK, Hoger A, McCulloch AD. Stress-dependent finite growth in soft elastic tissues. *J Biomech.* 1994;27:455-467.

[41] Sachs J, Text-book of Botany, Morphological and Physiological. Macmillan & Co, Oxford, 1875.

[42] Saksono PH, Peric D. On finite element modelling of surface tension. Variational formulation and applications. Part I: Quasistatic problems. *Comp Mech.* 2006;38:251-263.

[43] Simha NK, Bhattacharya K. Kinetics of phase boundaries with edges and junctions. *J Mech Phys Solids.* 1998;46:2323-2359.

[44] Socci L, Rennati G, Gervaso F, Vena P. An axisymmetric computational model of skin expansion and growth. *Biomech Model Mechanobiol.* 2007;6:177-188.

[45] Steigmann DJ, Ogden RW. Plane deformations of elastic solids with intrinsic boundary elasticity. *Proc R Soc Lond A.* 1997;453:853-877.

[46] Steigmann DJ, Ogden RW. A necessary condition for energy-minimizing plane deformations of elastic solids with intrinsic boundary elasticity. *Math Mech Solids.* 1997;2:3-16.

[47] Steinmann P. On boundary potential energies in deformational and configurational mechanics. *J Mech Phys Solids.* 2008;56:772-800.

[48] Suo Z. Motions of microscopic surfaces in materials. *Advances Appl Mech.* 19978;33:193-294.

[49] Taber LA. Biomechanics of growth, remodeling and morphogenesis. *Appl Mech Rev.* 1995;48:487-545.

[50] Taber LA, Humphrey JD. Stress-modulated growth, residual stress, and vascular heterogeneity. *J Biomech Eng.* 2001;123:528-535.

[51] Thimann KV, Schneider CL. Differential growth in plant tissues. *Am J Botany.* 1938;25:627-641.

[52] Tsamis A, Cheng A, Nguyen TC, Langer F, Miller DC, Kuhl E. Kinematics of cardiac growth - In vivo characterization of growth tensors and strains. *J Mech Behavior Biomed Mat.* 2012;8:165-177.

[53] Vandiver R, Goriely A. Tissue tension and axial growth of cylindrical structures in plants and elastic tissues. *EPL.* 2008;84:58004.p1-p6.

[54] Vandiver R, Goriely A. Differential growth and residual stress in cylindrical elastic structures. *Phil Trans R Soc A.* 2009;367:3607-3630.

[55] Wyczalkowski MA, Chen Z, Filas BA, Varner VD, Taber LA. Computational models for mechanics of morphogenesis. *Birth Defects Res C.* 2012;96:132-152.

[56] Xu G, Knutsen AK, Dikranian K, Kroenke CD, Bayly PV, Taber LA. Axons pull on the brain, but tension does not drive cortical folding. *J Biomech Eng.* 2010;132(7):071013.

[57] Young T. An essay on the cohesion of fluids. *Phil Trans R Soc London.* 1805;95:65-87.

[58] Zöllner AM, Buganza Tepole A, Kuhl E. On the biomechanics and mechanobiology of growing skin. *J Theor Bio*. 2012;297:166-175.

[59] Zöllner AM, Buganza Tepole A, Gosain AK, Kuhl E. Growing skin - Tissue expansion in pediatric forehead reconstruction. *Biomech Mod Mechanobio*. 2012;11:855-867.

[60] Zöllner AM, Abilez OJ, Böl M, Kuhl E. Stretching skeletal muscle: Chronic muscle lengthening through sarcomerogenesis. *PLoS ONE*. 2012;7(10):e45661.

RECENT REPORTS

12/95	On-Lattice Agent-based Simulation of Populations of Cells within the Open-Source Chaste Framework	Figueredo Joshi Osborne Byrne Owen
12/96	Mathematical Biomedicine and Modeling Avascular Tumor Growth	Byrne
12/97	Inference of the genetic network regulating lateral root initiation in Arabidopsis thaliana	Muraro Voß Wilson Bennett Byrne De Smet Hodgman King
12/98	Axisymmetric bifurcations of thick spherical shells under inflation and compression	deBotton Bustamante Dorfmann
12/99	Calculus from the past: Multiple Delay Systems arising in Cancer Cell Modelling	Wake Byrne
12/100	Nonlocal models of electrical propagation in cardiac tissue: electrotonic effects and the modulated dispersion of repolarization	Bueno-Orovio Kay Grau Rodriguez Burrage
12/101	Microfluidic Immunomagnetic Multi-Target Sorting A Model for Controlling Deflection of Paramagnetic Beads	Tsai Griffiths Stone
12/102	A New Lattice Boltzmann Equation to Simulate Density-Driven Convection of Carbon Dioxide	Allen Reis Sun
12/103	Control and optimization of solute transport in a porous tube	Griffiths Howell Shipley
12/104	Air-cushioning in impact problems	Moore Ockendon Oliver
12/105	Strain controlled biaxial stretch: An experimental characterization of natural rubber	Pancheri Dorfmann
12/106	Non-linear modeling of active biohybrid materials	Paetsch Dorfmann
12/107	Coalescence of Liquid Drops: Different Models Versus Experiment	Sprittles Shikhmurzaev
12/108	Adjoint Based A Posteriori Analysis of Multiscale Mortar Discretizations with Multinumerics	Tavener Wildey

12/109	Dynamics of mechanically induced fiber reorientation in the material reinforced by two families of fibers	Melnik Goriely
12/110	Multiscale stochastic reaction-diffusion modelling: application to actin dynamics in filopodia	Erban Flegg Papoian
12/111	Exploiting the Synergy Between Carboplatin and ABT-737 in the Treatment of Ovarian Carcinomas	Jain Richardson Meyer-Hermann Byrne
12/112	The integration of hormonal signaling networks and mobile microRNAs is required for vascular patterning in Arabidopsis roots	Muraro Pound Help Lucas Chopard Byrne Godin Hodgman King Pridmore Helariutta Bennett Bishopp
12/113	Fast solution of Cahn-Hilliard Variational Inequalities using Implicit Time Discretization and Finite Elements	Bosch Stoll Benner
12/114	An Embedding Technique for the Solution of Reaction-Diffusion Equations on Algebraic Surfaces with Isolated Singularities	Rockstroh März Ruuth
12/115	Mathematicians at the Movies: Sherlock Holmes vs. Professor Moriarty	Moulton Goriely
13/01	Rotation, inversion, and perversion in anisotropic elastic cylindrical tubes and membranes	Goriely Tabor
13/02	Drop spreading and penetration into pre-wetted powders	Marston Sprittles Zhu Li Vakarelski Thoroddsen

Copies of these, and any other OCCAM reports can be obtained from:

Oxford Centre for Collaborative Applied Mathematics
Mathematical Institute
24 - 29 St Giles'
Oxford
OX1 3LB
England
www.maths.ox.ac.uk/occam